



# A metal-organic framework that exhibits CO<sub>2</sub>-induced transitions between paramagnetism and ferrimagnetism

Jun Zhang<sup>1,2</sup>, Wataru Kosaka<sup>1,2</sup>, Yasutaka Kitagawa<sup>1,3</sup> and Hitoshi Miyasaka<sup>1,2</sup>✉

**With adequate building blocks, metal-organic frameworks (MOFs) can combine magnetic ordering and porosity. This makes MOFs a promising platform for the development of stimulus-responsive materials that show drastically different magnetic properties depending on the presence or absence of guest molecules within their pores. Here we report a CO<sub>2</sub>-responsive magnetic MOF that converts from ferrimagnetic to paramagnetic on CO<sub>2</sub> adsorption, and returns to the ferrimagnetic state on CO<sub>2</sub> desorption. The ferrimagnetic material is a layered MOF with a [D<sup>+</sup>-A<sup>-</sup>-D] formula, produced from the reaction of trifluorobenzoate-bridged paddlewheel-type diruthenium(II) clusters as the electron donor (D) with diethoxytetracyanoquinodimethane as the electron acceptor (A). On CO<sub>2</sub> uptake, it undergoes an in-plane electron transfer and a structural transition to adopt a [D-A-D] paramagnetic form. This magnetic phase change, and the accompanying modifications to the electronic conductivity and permittivity of the MOF, are electronically stabilized by the guest CO<sub>2</sub> molecules accommodated in the framework.**

Switchable magnets, with magnetic properties that can be reversibly changed in response to external stimuli, have promising potential for applications such as specific stimulus-responsive switches, memories and sensors<sup>1-4</sup>. The magnetic variability of these materials results from the high flexibility of their electronic states and structures<sup>4</sup>. There are several types of switchable magnets, mostly based on molecular materials<sup>5</sup>, which are driven by various stimuli. Materials were prepared that show a direct response to intrinsic electronic state changes, such as photoirradiations<sup>6</sup>, electric currents<sup>7</sup> and electric fields<sup>8</sup>, but also to the insertion and extraction of guests, such as water<sup>9-12</sup> and organic molecules<sup>13-20</sup>, as well as guest-responsive spin-crossover materials<sup>21-24</sup>. The latter examples are porous magnets that combine porosity and magnetic ordering in metal-organic frameworks (MOFs)<sup>25</sup>, also referred to as porous coordination polymers<sup>26</sup>. Ubiquitous gases, such as nitrogen (N<sub>2</sub>), oxygen (O<sub>2</sub>) and carbon dioxide (CO<sub>2</sub>) are some of the most attractive targets for adsorption, but they only interact weakly with MOFs. Therefore, great efforts have been made to enhance the interactions by utilizing nanometric pores<sup>24</sup>, open metal sites<sup>18,19</sup> and the spin of the paramagnetic gas<sup>20</sup>. However, to obtain a selective and large magnetic response to gas sorption has remained challenging.

An effective method to induce a drastic magnetic phase change is by manipulating electronic states in strongly correlated electronic systems. For this, a guest-responsive magnetic material whose building blocks can undergo a change in charge<sup>15</sup> is a suitable material, as it concomitantly undergoes in-plane electron transfer, which involves a change of intrinsic spin states and their magnetic correlations. Here we report a gas-responsive magnet that is a paramagnet on CO<sub>2</sub> adsorption (with its magnetism 'switched off') and converts into a ferrimagnet on CO<sub>2</sub> desorption (with its magnetism now 'switched on'). The as-synthesized porous magnet is a layered MOF that consists of trifluorobenzoate-bridged paddlewheel-type ruthenium(II) dimers as electron donors (D) coordinated in-plane to 2,5-diethoxy-7,7,8,8-tetracyanoquinodimethane (TCNQ(OEt)<sub>2</sub>)

units as the electron acceptor (A) (Fig. 1a). This produces a ferrimagnetic material through a one-electron-transferred form of [D-A<sup>-</sup>-D<sup>+</sup>]<sub>∞</sub>. This electron transfer happens through strong superexchange interactions between the paramagnetic D (S = 1 for a [Ru<sup>II</sup>, Ru<sup>III</sup>] cluster) and D<sup>+</sup> (S = 3/2 for a [Ru<sup>II</sup>, Ru<sup>III</sup>]<sup>+</sup> cluster) subunits via A<sup>-</sup> with S = 1/2 (TCNQ(OEt)<sub>2</sub><sup>-</sup>). Once the CO<sub>2</sub> is adsorbed stepwise within and between layers, the [D-A<sup>-</sup>-D<sup>+</sup>] framework undergoes a magnetic and structural phase transition that involves an intralattice electron transfer of D<sup>+</sup> ← A<sup>-</sup> to produce a paramagnetic neutral form of [D-A-D]<sub>∞</sub> with a diamagnetic A.

Recently, CO<sub>2</sub> has drawn particular attention because of the global environmental problems associated with the ever-increasing CO<sub>2</sub> levels in the atmosphere<sup>27,28</sup>. As MOFs have long attracted interest for the potential of their porous domains for practical applications<sup>29-31</sup>, which include as storage materials<sup>32,33</sup>, separators<sup>34,35</sup> and reduction catalysts<sup>36,37</sup>, we feel that CO<sub>2</sub>-responsive materials are particularly interesting.

## Results and discussion

**As-synthesized MOF and its desolvated counterpart.** A D<sub>2</sub>A-layered ferrimagnet, [(Ru<sub>2</sub>(F<sub>3</sub>PhCO<sub>2</sub>)<sub>4</sub>)<sub>2</sub>TCNQ(OEt)<sub>2</sub>]<sub>2</sub>·3D CM (**1-DCM**; F<sub>3</sub>PhCO<sub>2</sub><sup>-</sup>, 2,4,6-trifluorobenzoate; DCM, dichloromethane) was obtained from a D:A = 2:1 assembly of the paddlewheel-type [Ru<sub>2</sub>(F<sub>3</sub>PhCO<sub>2</sub>)<sub>4</sub>] complex ([Ru<sub>2</sub>]) as D and TCNQ(OEt)<sub>2</sub> as A (Fig. 1a)<sup>38,39</sup>. Compound **1-DCM** crystallized in the monoclinic C2/c space group (Supplementary Fig. 1 and Supplementary Table 1), in which the four CN groups of TCNQ(OEt)<sub>2</sub> coordinated with the [Ru<sub>2</sub>] units to form a fishnet-like two-dimensional network that lies on the (020) plane (Fig. 1b). The bond lengths in the [Ru<sub>2</sub>] and TCNQ(OEt)<sub>2</sub> moieties characterized the one-electron-transferred state with a charge assignment of [-{Ru(1)<sup>II</sup>, Ru(1)<sup>III</sup>}-μ<sub>4</sub>-TCNQ(OEt)<sub>2</sub><sup>-</sup>-{Ru(2)<sup>II</sup>, Ru(2)<sup>III</sup>}<sup>+</sup>] in **1-DCM** (Supplementary Fig. 3 and Supplementary Tables 2 and 3). The layers were stacked in a staggered manner along the b axis with a

<sup>1</sup>Institute for Materials Research, Tohoku University, Sendai, Japan. <sup>2</sup>Department of Chemistry, Graduate School of Science, Tohoku University, Sendai, Japan. <sup>3</sup>Department of Materials Engineering Science, Graduate School of Engineering Science, Osaka University, Toyonaka, Japan. ✉e-mail: [miyasaka@imr.tohoku.ac.jp](mailto:miyasaka@imr.tohoku.ac.jp)

vertical distance of 8.83 Å (Supplementary Fig. 2). Meanwhile, the crystallization solvents (3DCM) were located at the centre of the hexagonal pore of the fishnet (Fig. 1c) with a solvent-accessible volume of 1,270.4 Å<sup>3</sup> (317.6 Å<sup>3</sup> per formula unit, 15.4% of the total volume).

Compound **1-DCM** released DCM molecules on heating to produce the solvent-free compound  $[\{\text{Ru}_2(\text{F}_3\text{PhCO}_2)_4\}_2\text{TCNQ}(\text{OEt})_2]$  (**1**), which was stable at temperatures up to 473 K (Supplementary Fig. 4) with its crystallinity intact. Compound **1** crystallized in the triclinic *P*1 space group (*Z* = 1; Supplementary Fig. 1 and Supplementary Table 1). The fishnet network was preserved, lying on the (020) plane, with the transformed axis vectors **a'**, **b'** and **c'** indicated for an easier comparison of the structure of **1** (Fig. 1d,e) with **1-DCM**, with the (111) plane lying in the original cell. The layers were stacked in a staggered manner along the **b'** axis (the [101] direction in the original cell) with a shortened interlayer distance of 8.07 Å compared with that in **1-DCM** (Supplementary Fig. 2). The bonding form of the D:A building subunits in **1-DCM** was drastically altered to form **1**, changing from an almost flat layer in **1-DCM** to a wavy layer in **1**, which effectively reduced the void space for solvent accommodation to a void volume of 32.9 Å<sup>3</sup> (1.9% of the total volume), which resulted in a non-porous packing structure in **1** (Fig. 1a–d and Supplementary Table 4). The overall electronic state of **1** remained unchanged as a one-electron-transferred state, although the electronic states of the respective  $[\text{Ru}_2]$  units switched as  $[-\{\text{Ru}(1)^{\text{II}}, \text{Ru}(1)^{\text{III}}\}^+ - \mu_4\text{-TCNQ}(\text{OEt})_2\text{-}\{\text{Ru}(2)^{\text{II}}, \text{Ru}(2)^{\text{III}}\}^-]$  (Supplementary Fig. 3 and Supplementary Tables 2 and 3), which suggests the presence of flexible charge states in this material. Compound **1** returned to **1-DCM** after being exposed to a DCM vapour (Supplementary Figs. 5 and 6), which acts as a general magnetic sponge (vide infra).

In both **1-DCM** and **1**, the spins of the  $[\text{Ru}^{\text{II}}, \text{Ru}^{\text{III}}]$  (*S* = 1) and  $[\text{Ru}^{\text{II}}, \text{Ru}^{\text{III}}]^+$  (*S* = 3/2) moieties antiferromagnetically interacted with the radical *S* = 1/2 spin of  $\text{TCNQ}(\text{OEt})_2^-$  over the layered network. This resulted in a ferrimagnetically ordered layer being formed, followed by three-dimensional ferrimagnetic ordering because of the interlayer ferromagnetic interactions. The cooling process of the magnetic susceptibility ( $\chi$ ) of **1-DCM** and **1** that was measured at  $H_{\text{dc}} = 1$  kOe showed an abrupt increase at approximately 90–110 K (Fig. 1f, Supplementary Figs. 7 and 8), indicating the onset of ferrimagnetic ordering, with  $T_{\text{C}}$  (Curie temperature) = 88 K and 110 K for **1-DCM** and **1**, respectively (inset of Fig. 1f), as shown in their ac susceptibility data (Supplementary Figs. 7 and 8). The change in  $T_{\text{C}}$  should be ascribed to the change in local geometries around the  $[\text{Ru}_2]^{0/+}$  subunits and  $\text{TCNQ}(\text{OEt})_2^-$  (Supplementary Table 4) and their interlayer distances. The saturated magnetization ( $M_{\text{s}}$ ) values at  $H_{\text{dc}} = 7$  T of **1-DCM** and **1** were  $1.09 \times 10^4$  emu G mol<sup>-1</sup> ( $1.95 N\mu_{\text{B}}$ ) and  $1.16 \times 10^4$  emu G mol<sup>-1</sup> ( $2.08 N\mu_{\text{B}}$ ), respectively (Fig. 1g). The large hysteresis loops with coercive fields ( $H_{\text{c}}$ ) of 1.56 T and 2.45 T for **1-DCM** and **1**, respectively (Supplementary Figs. 7 and 8), implied the existence of a large magnetic anisotropy, which arises from the features of the  $[\text{Ru}_2]$  subunits and layers in these compounds<sup>38,39</sup>. This magnetic sponge behaviour is reversibly switchable without degradation in the adsorption/desorption cycles (Supplementary Fig. 9).

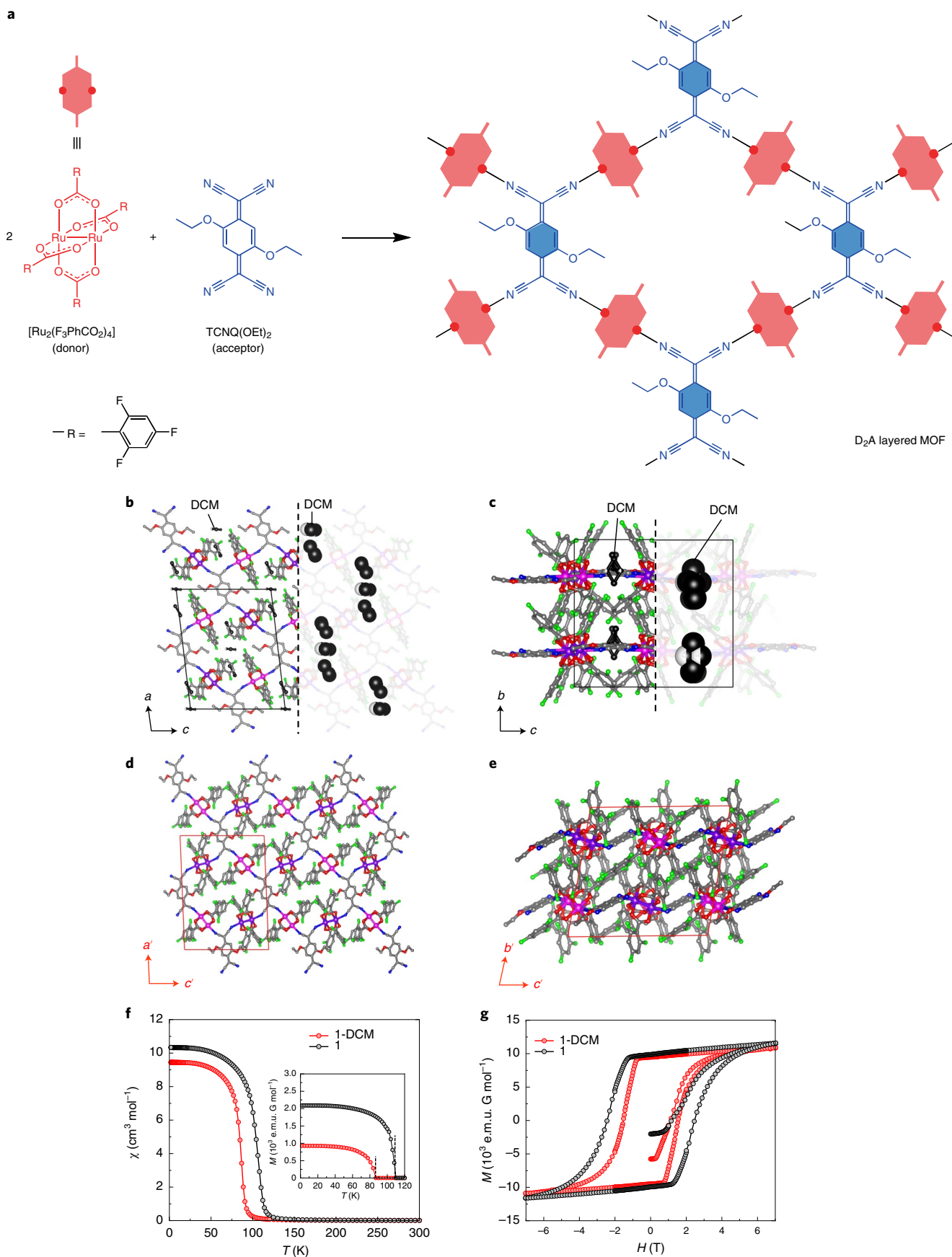
**CO<sub>2</sub> sorption behaviour.** The CO<sub>2</sub> sorption isotherms for **1** were measured at several temperatures (Fig. 2a and Supplementary Fig. 10) and revealed a gated sorption behaviour. At 195 K, the isotherm showed a sharp rise at approximately 1.1 kPa CO<sub>2</sub> pressure ( $P_{\text{CO}_2}$ ), which resulted in the first gate-opening (1st GO) transition, and on increasing the CO<sub>2</sub> pressure to  $P_{\text{CO}_2} = 5.2$  kPa, another abrupt increase occurred, the second gate-opening (2nd GO) transition required to reach an adsorbed amount of 113 mlSTP g<sup>-1</sup> (10.6 molecules per formula unit) at 99 kPa (Fig. 2a). The GO pressure (and gate-closing (GC) pressure) steadily increased with temperature increase, and then the 2nd GO (GC) eventually disappeared above 230 K in the CO<sub>2</sub> pressure range below 100 kPa (Fig. 2a and Supplementary Fig. 10). The temperature dependence of the GO and GC pressures obeyed the Clausius–Clapeyron relationship,  $d(\ln(P))/d(T^{-1}) = \Delta H_{\text{Trans}}/R_{\text{g}}$ , where  $\Delta H_{\text{Trans}}$  is the variation in the transition enthalpy and  $R_{\text{g}}$  is the gas constant (Fig. 2c and Supplementary Figs. 10 and 12)<sup>40</sup>. The estimates of  $\Delta H_{\text{Trans}}$  were –24.7, –34.4, –27.9 and –29.4 kJ mol<sup>-1</sup> for the 1st GO, 2nd GO, 1st GC and 2nd GC, respectively. The gated behaviour was also characterized in the isobar plots (Fig. 2b and Supplementary Fig. 10). However, the 1st GO isobar behaviour was characteristically different as it occurred gradually and stepwise over a wide temperature range defined by an initial GO (1st GO-i) and an ending GO (1st GO-e), which appeared at higher and lower temperatures than the 1st GO in the isotherm, respectively ( $\Delta H_{\text{Trans}} = -28.6$  and  $-22.5$  kJ mol<sup>-1</sup> for the 1st GO-i and 1st GO-e, respectively; Supplementary Fig. 14). Meanwhile, the GC behaviour in the isobars was the same as that in the isotherms. Such gating behaviours were investigated by CO<sub>2</sub>-atmosphere-controlled in situ powder X-ray diffraction (PXRD) measurements at several temperatures (Fig. 2d and Supplementary Fig. 10). We demonstrated that two different CO<sub>2</sub>-adsorbed phases existed: **1DCO<sub>2</sub>-I** and **1DCO<sub>2</sub>-II** in the ranges  $298 \leq T \leq 250$  K and  $210 \leq T \leq 195$  K, respectively, at  $P_{\text{CO}_2} = 100$  kPa, with a mixture that existed over the 220–230 K range. Meanwhile, the desorption process transition behaviour was thoroughly investigated (Supplementary Fig. 15), which revealed that the structural transformations from **1DCO<sub>2</sub>-I** to **1** and from **1DCO<sub>2</sub>-II** to **1DCO<sub>2</sub>-I** were associated with the 1st and 2nd GC steps, respectively (Supplementary Fig. 16). Based on these data, the phase diagram of **1** under CO<sub>2</sub> was created for the GO and GC processes ( $T$ – $P_{\text{CO}_2}$  plots in Fig. 2c and Supplementary Fig. 10c, respectively). Differential scanning calorimetry was conducted for the cooling and heating processes in the 200–330 K temperature range under a CO<sub>2</sub> atmosphere (Fig. 2e). The results showed two couples of exo/endothemic peaks that correspond to the aforementioned structural transformations with temperature hysteresis between the cooling and heating processes (7 K for 1st GO/GC of the **1DCO<sub>2</sub>-I/1** transition and 12 K for 2nd GO/GC of the **1DCO<sub>2</sub>-II/1DCO<sub>2</sub>-I** transition), and thereby revealed the first-order nature of the phase transition.

**Characterization of CO<sub>2</sub>-accommodated phases.** The crystal structures of **1DCO<sub>2</sub>-I** and **1DCO<sub>2</sub>-II** were determined by the CO<sub>2</sub>-atmosphere-controlled in situ single-crystal X-ray diffraction analyses. The **1DCO<sub>2</sub>-I** phase ( $P_{\text{CO}_2} \approx 3$  kPa), which was isostructural with **1-DCM**, crystallized in the monoclinic *C2/c* space group

**Fig. 1 | Structural modulation and magnetic sponge behaviour during the solvation and desolvation process.** **a**, Schematic representation of the assembly reaction between  $[\text{Ru}_2(\text{F}_3\text{PhCO}_2)_4]$  as the electron-donor (D) and  $\text{TCNQ}(\text{OEt})_2$  as the electron acceptor (A) to form a D<sub>2</sub>A layered MOF. Only part of the paddlewheel cluster is shown. **b–e**, Packing views of **1-DCM** along the *b* (**b**) and *a* (**c**) crystallographic axes and views of **1** along the *b'* (**d**) and *a'* (**e**) crystallographic axes. N, blue; O, red; C, grey; F, green; Ru in  $[\text{Ru}^{\text{II}}, \text{Ru}^{\text{III}}]$ , pink; Ru in  $[\text{Ru}^{\text{II}}, \text{Ru}^{\text{III}}]^+$ , purple. The DCM molecules shown in **b** and **c** are represented in black and white. The right side of **b** and **c** emphasizes the DCM molecules in a CPK model, and the bicouleur (black and white) shows occupancy disorder over two sites for the DCM molecules. The hydrogen atoms are omitted for clarity, and only one layer is depicted in **b** and **d** for clarity. **f**, Temperature dependence of the magnetic susceptibility ( $\chi$ ) for **1-DCM** and **1** measured under a 1 kOe d.c. field ( $H_{\text{dc}}$ ) in a field-cooled process. Inset: remnant magnetization at  $H_{\text{dc}} = 0$  Oe (heating process), measured after taking a field-cooled magnetization under a 5 Oe d.c. field, in which the vertical lines indicate the respective  $T_{\text{C}}$ . **g**, *M*–*H* curves of **1-DCM** and **1** (black) at 1.8 K.

( $Z=4$ ) with the same one-electron-transferred electronic state as **1-DCM** (Fig. 3a,b, Supplementary Figs. 17–20 and Supplementary Tables 1–3). Its structural feature can be considered as the DCM

molecules in **1-DCM** replaced by four molar amounts of  $\text{CO}_2$  molecules in **1-DCO<sub>2</sub>-I**, that is, a pseudopolymorph, in which  $\text{CO}_2$  is located at the centre of the hexagonal fishnet (cyan in Fig. 3a,b).



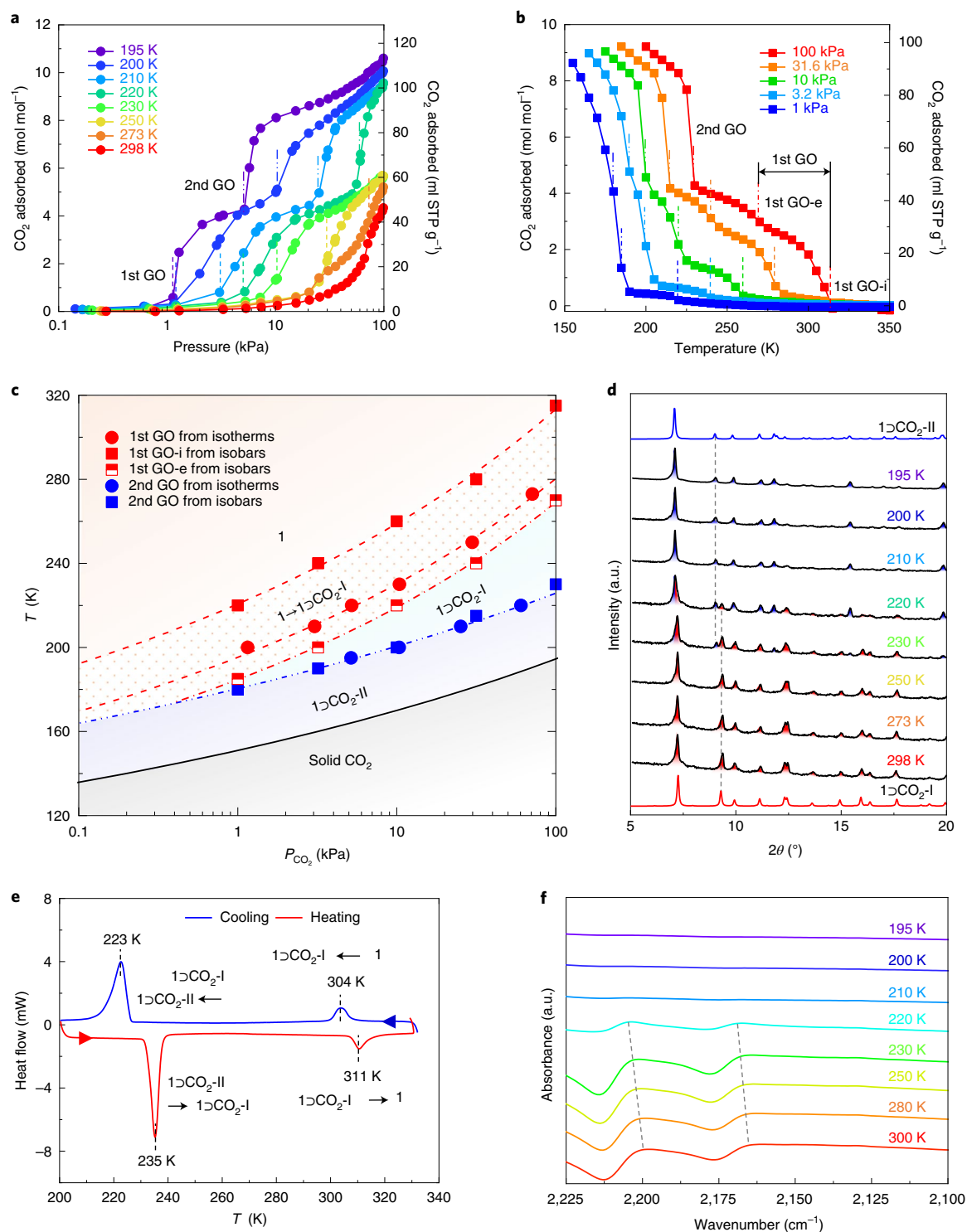


**Fig. 2 | CO<sub>2</sub> adsorption, variation of crystal structures and infrared spectra for compound 1.** **a, b**, CO<sub>2</sub> adsorption isotherms (**a**) and isobars (**b**) of **1** at various temperatures (solid lines are a guide for the eye). **c**, Phase diagrams for **1**, **1CO<sub>2</sub>-I** and **1CO<sub>2</sub>-II** determined from CO<sub>2</sub> adsorption isotherms and isobars. The red and blue dotted lines represent the fitting based on the Clausius–Clapeyron equation (Supplementary Figs. 12 and 14). The black solid line represents the saturated vapour pressure curve, and distinguishes between the gas and solid phases for bulk CO<sub>2</sub>. **d**, PXRD patterns measured under  $P_{\text{CO}_2} = 100$  kPa at various temperatures on cooling. The simulated patterns for **1CO<sub>2</sub>-I** and **1CO<sub>2</sub>-II** from single-crystal X-ray structural analyses are shown by red and blue lines, respectively. **e**, Temperature dependence of heat flow in differential scanning calorimetry for **1** under a CO<sub>2</sub> flow of 50 ml min<sup>-1</sup> (general atmosphere pressure) with a temperature sweep rate of 5 K min<sup>-1</sup>. **f**, Infrared spectra of **1** measured under  $P_{\text{CO}_2} = 100$  kPa at various temperatures (as indicated) on cooling. a.u., arbitrary units.

The **1CO<sub>2</sub>-II** phase ( $P_{\text{CO}_2} \approx 100$  kPa) crystallized in the triclinic  $P\bar{1}$  space group ( $Z = 1$ ) (Supplementary Fig. 17 and Supplementary Table 1) with the largest volume and guest-accessible void per

formula unit among the phases, when compared with a temporary unit cell with the transformed axis vectors  $\mathbf{a}'$ ,  $\mathbf{b}'$  and  $\mathbf{c}'$  (Fig. 3c,d and Supplementary Table 4). The CO<sub>2</sub> molecules (about four)

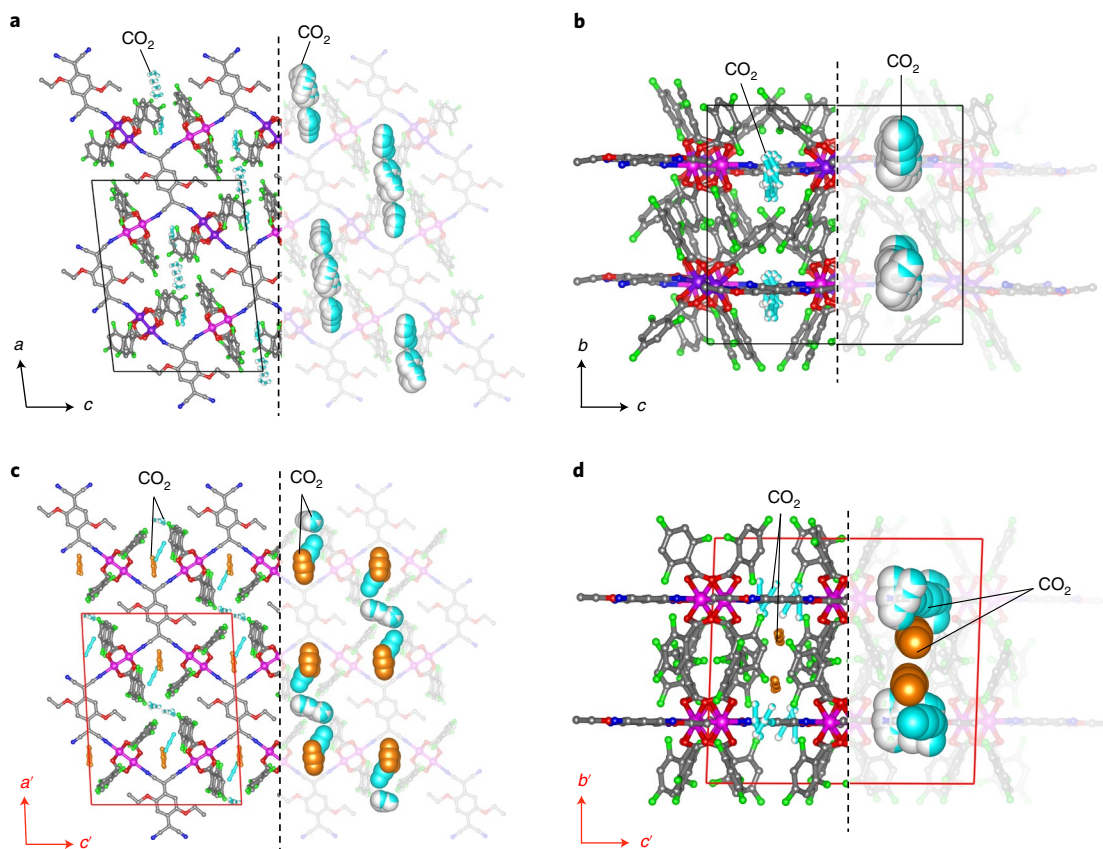


**Fig. 3 | Crystal structures of CO<sub>2</sub>-accommodated phases.** **a,b**, Crystal structures of **1DCO<sub>2</sub>-I** viewed along the *b*-axis (**a**) and the *a*-axis (**b**). **c,d**, Crystal structures of **1DCO<sub>2</sub>-II** viewed along the *b'*-axis (**c**) and the *a'*-axis (**d**). N, blue; O, red; C, grey; F, green; Ru in [Ru<sup>II</sup>, Ru<sup>III</sup>], pink; Ru in [Ru<sup>II</sup>, Ru<sup>III</sup>]<sup>+</sup>, purple. Hydrogen atoms are omitted for clarity. The right sides of the panels emphasize the adsorbed CO<sub>2</sub> molecules associated with the 1st and 2nd GO in the CPK models in cyan/white and orange, respectively; the bicolour (cyan/white) shows occupancy disorder over two sites for the 1st GO CO<sub>2</sub> molecules.

further accommodated in **1DCO<sub>2</sub>-II** from **1DCO<sub>2</sub>-I** were loaded in the void space newly produced between the layers by the structural transition (orange in Fig. 3c,d and Supplementary Figs. 18 and 19). The **1DCO<sub>2</sub>-II** D<sub>2</sub>A layer became flatter than the **1DCO<sub>2</sub>-I** layer (Fig. 3), which resulted from a reduction in the twisted angle ( $\varphi$ ) on the TCNQ(OEt)<sub>2</sub> and Ru–N–C bending angle ( $\delta$ ) (Supplementary Tables 4 and 5). The most striking feature of **1DCO<sub>2</sub>-II** was that the electronic state turned into the neutral state with the formula [–{Ru(1)<sup>II</sup>, Ru(1)<sup>III</sup>}–TCNQ(OEt)<sub>2</sub><sup>0</sup>–{Ru(2)<sup>II</sup>, Ru(2)<sup>III</sup>}–] (Supplementary Fig. 20 and Supplementary Tables 2 and 3). Basically,  $\varphi$  should be nearly zero for the neutral state of TCNQ(OEt)<sub>2</sub>, whereas it increased in TCNQ(OEt)<sub>2</sub><sup>2–</sup> (Supplementary Table 5)<sup>9</sup>. Therefore, the structural correction to the highly flat form of the TCNQ(OEt)<sub>2</sub> moiety induced by the further accommodation of CO<sub>2</sub> in **1DCO<sub>2</sub>-II** could have resulted in the formation of the neutral state.

The electronic state change was monitored in the C≡N stretching mode ( $\nu_{\text{C}\equiv\text{N}}$ ) of TCNQ(OEt)<sub>2</sub> based on the CO<sub>2</sub>-atmosphere-controlled in situ infrared spectra measurements (Fig. 2f and Supplementary Figs. 10 and 21). The two  $\nu_{\text{C}\equiv\text{N}}$  bands at 2,195 cm<sup>–1</sup> and 2,161 cm<sup>–1</sup> for **1-DCM** and 2,180 cm<sup>–1</sup> and 2,131 cm<sup>–1</sup> for **1** were both observed at lower frequencies than those of the original neutral TCNQ(OEt)<sub>2</sub> (2,217 cm<sup>–1</sup> and 2,208 cm<sup>–1</sup>, respectively), which indicates a reduction in TCNQ(OEt)<sub>2</sub> (ref. 41). Meanwhile, when **1** was cooled from 300 to 195 K under  $P_{\text{CO}_2}$  = 100 kPa, an apparent spectral change was observed (Fig. 2f). The  $\nu_{\text{C}\equiv\text{N}}$  bands at 2,204 cm<sup>–1</sup> and 2,169 cm<sup>–1</sup> at 300 K, which were like those of **1-DCM**, indicated the presence of the one-electron-transferred state in **1DCO<sub>2</sub>-I**. On cooling, both the  $\nu_{\text{C}\equiv\text{N}}$  bands became broad and weakened at

around 230 K, in line with the charge variation from TCNQ(OEt)<sub>2</sub><sup>–</sup> (one-electron-transferred state) in **1DCO<sub>2</sub>-I** to TCNQ(OEt)<sub>2</sub><sup>0</sup> (neutral state) in **1DCO<sub>2</sub>-II** (ref. 41), which is consistent with the results from the Raman spectra (Supplementary Fig. 22). This variation of  $\nu_{\text{C}\equiv\text{N}}$  bands in the infrared spectra was also observed at 195 K under various CO<sub>2</sub> pressures (Supplementary Fig. 21).

**Changes in magnetic and electronic properties induced by CO<sub>2</sub> adsorption and desorption.** The drastic change in electronic state between the neutral and one-electron-transferred states resulted in a magnetic phase change because of the spin state change from the ferrimagnetic spin arrangement of [(*S* = 1 for {Ru<sup>II</sup>, Ru<sup>III</sup>})–(*S* = 1/2 for TCNQ(OEt)<sub>2</sub><sup>–</sup>)–(*S* = 3/2 for {Ru<sup>II</sup>, Ru<sup>III</sup>})] for the one-electron-transferred state to the paramagnetic spin arrangement of [(*S* = 1 for {Ru<sup>II</sup>, Ru<sup>III</sup>})–(*S* = 0 for TCNQ(OEt)<sub>2</sub><sup>0</sup>)–(*S* = 1 for {Ru<sup>II</sup>, Ru<sup>III</sup>})] for the neutral state. After checking for ferrimagnetic behaviour at *T*<sub>c</sub> = 110 K in **1** by measuring the field-cooled magnetization under vacuum using a homemade sealed cell. CO<sub>2</sub> gas at  $P_{\text{CO}_2}$  = 10, 50 and 100 kPa was introduced into the cell<sup>16</sup> at 300 K, and the *M*–*T* curves for the cooling and heating processes were measured at *H*<sub>dc</sub> = 1 kOe (Fig. 4a). The spontaneous magnetization disappeared under  $P_{\text{CO}_2}$  = 10 kPa as well as under  $P_{\text{CO}_2}$  = 50 kPa and 100 kPa (Fig. 4a), but was recovered by evacuating the CO<sub>2</sub>. By repeating the CO<sub>2</sub> introduction/evacuation process, the magnetic phase was reversibly switched several times at temperatures below 110 K (= *T*<sub>c</sub> for **1**) between paramagnetism and ferrimagnetism without degradation (Fig. 4c and Supplementary Fig. 23). An abrupt change in *M* was observed in each temperature-sweep process with the temperature

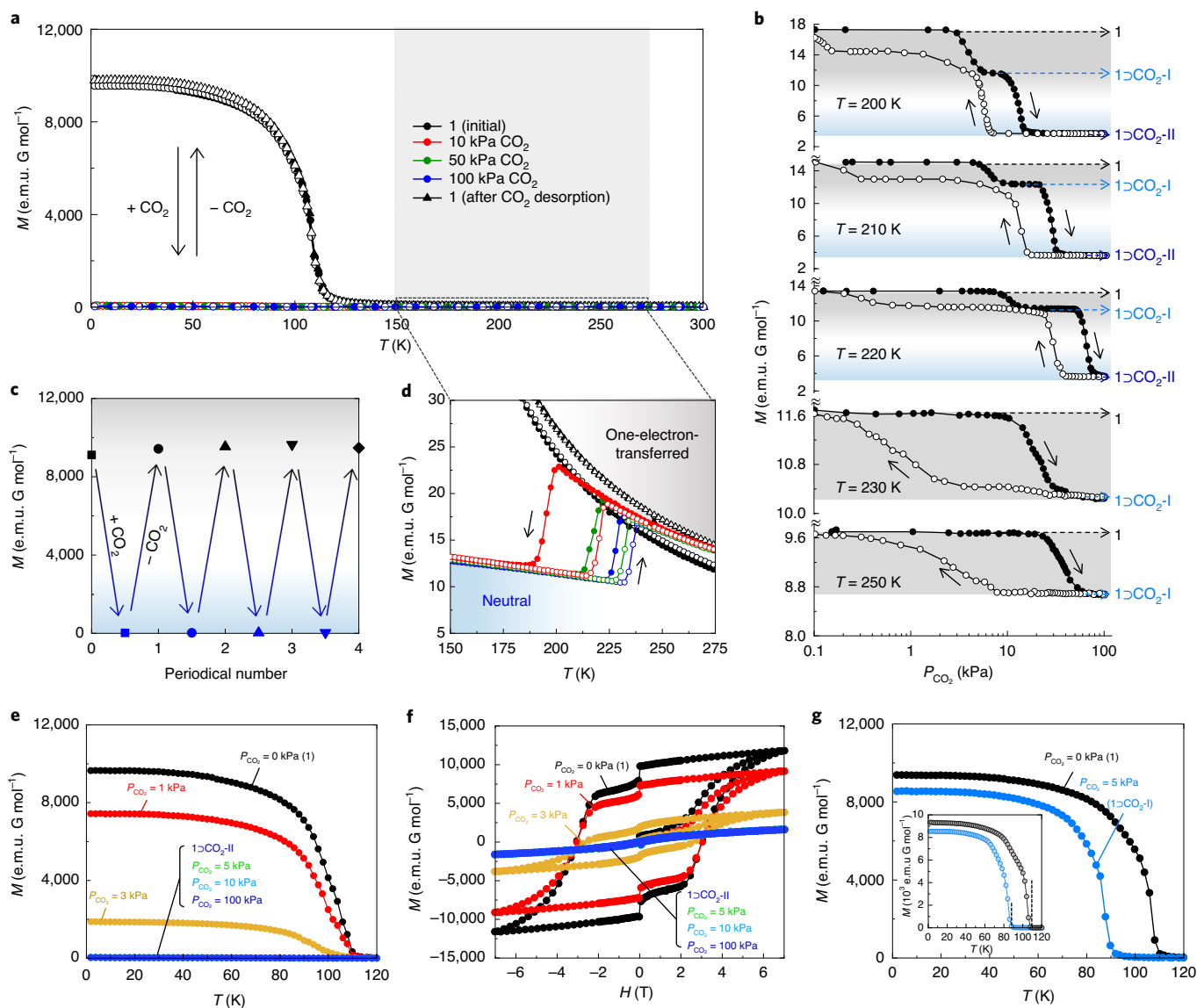


**Fig. 4 | Variation of magnetic properties under CO<sub>2</sub> adsorption.** **a**, The CO<sub>2</sub> pressure dependence of  $M$ - $T$  curves at  $H_{dc}=1$  kOe for **1** during cooling (filled symbols) and heating (open symbols) processes. **b**, Magnetization variation as a function of CO<sub>2</sub> pressure during adsorption (filled symbols) and desorption (open symbols) processes at a fixed temperature in the range 200–250 K. **c**, The reversible variation of magnetization at  $T=1.8$  K at  $H_{dc}=100$  Oe on CO<sub>2</sub> desorption/adsorption cycles ( $P_{CO_2}=100$  kPa at 300 K). **d**, A magnified view of the  $M$ - $T$  curves where the phase transition between **1**>CO<sub>2</sub>-I and **1**>CO<sub>2</sub>-II occurs. **e**, The CO<sub>2</sub> pressure dependence of field-cooled magnetization curves measured with a temperature sweep rate of 1 K min<sup>-1</sup> at a magnetic field of 100 Oe. **f**,  $M$ - $H$  curves at 1.8 K measured under several CO<sub>2</sub> pressures with a temperature sweep rate of 1 K min<sup>-1</sup>. **g**, Rapidly cooled magnetization curves with a temperature sweep rate of 10 K min<sup>-1</sup> at a magnetic field of 100 Oe under  $P_{CO_2}=5$  kPa (blue) and 0 kPa (black). Inset: temperature dependence of remnant magnetization.

hysteresis phenomenon in the cooling/heating processes as shown in Fig. 4d, which is associated with the phase transition between **1**>CO<sub>2</sub>-I and **1**>CO<sub>2</sub>-II (Supplementary Fig. 25). The CO<sub>2</sub> introduced into the ferrimagnet **1** at 300 K generated the **1**>CO<sub>2</sub>-I phase, but with the same one-electron-transferred state, and its magnetization followed almost the same trend as that of **1** until a temperature of approximately 230 K ( $P_{CO_2}=100$  kPa) was reached in the cooling process. On further cooling, the phase transition to **1**>CO<sub>2</sub>-II occurred at a temperature ( $T_{IN}$ ) as a result of the electronic state change from the one-electron-transferred state to the neutral state, which corresponded to the paramagnetism of the isolated  $S=1$  spins for the two [Ru<sup>II</sup>, Ru<sup>III</sup>] subunits. Thus, **1**>CO<sub>2</sub>-II behaved paramagnetically at lower temperatures than  $T_{IN}$ . These stepwise changes could easily be

realized from the  $M$  variation as a function of CO<sub>2</sub> pressure at a fixed temperature (Fig. 4b). Two-step changes with adsorption/desorption hysteresis were observed in the temperature range 200–220 K. This corresponded to the phase transitions from **1** to **1**>CO<sub>2</sub>-I, that is, a small change attributed to a structural modification of the 1st GO, and from **1**>CO<sub>2</sub>-I to **1**>CO<sub>2</sub>-II, that is, a large change due to electron transfer in the 2nd GO, for the adsorption process and vice versa for the desorption (Supplementary Figs. 26–28). Only a small change in  $M$  with the adsorption/desorption hysteresis, which corresponded to the transition between **1** and **1**>CO<sub>2</sub>-I in the 1st GO/GC processes, was observed at 230 K and at 250 K (Supplementary Figs. 29 and 30). These changes agree with the phase diagrams in Fig. 2c and Supplementary Fig. 10c (Supplementary Fig. 31).

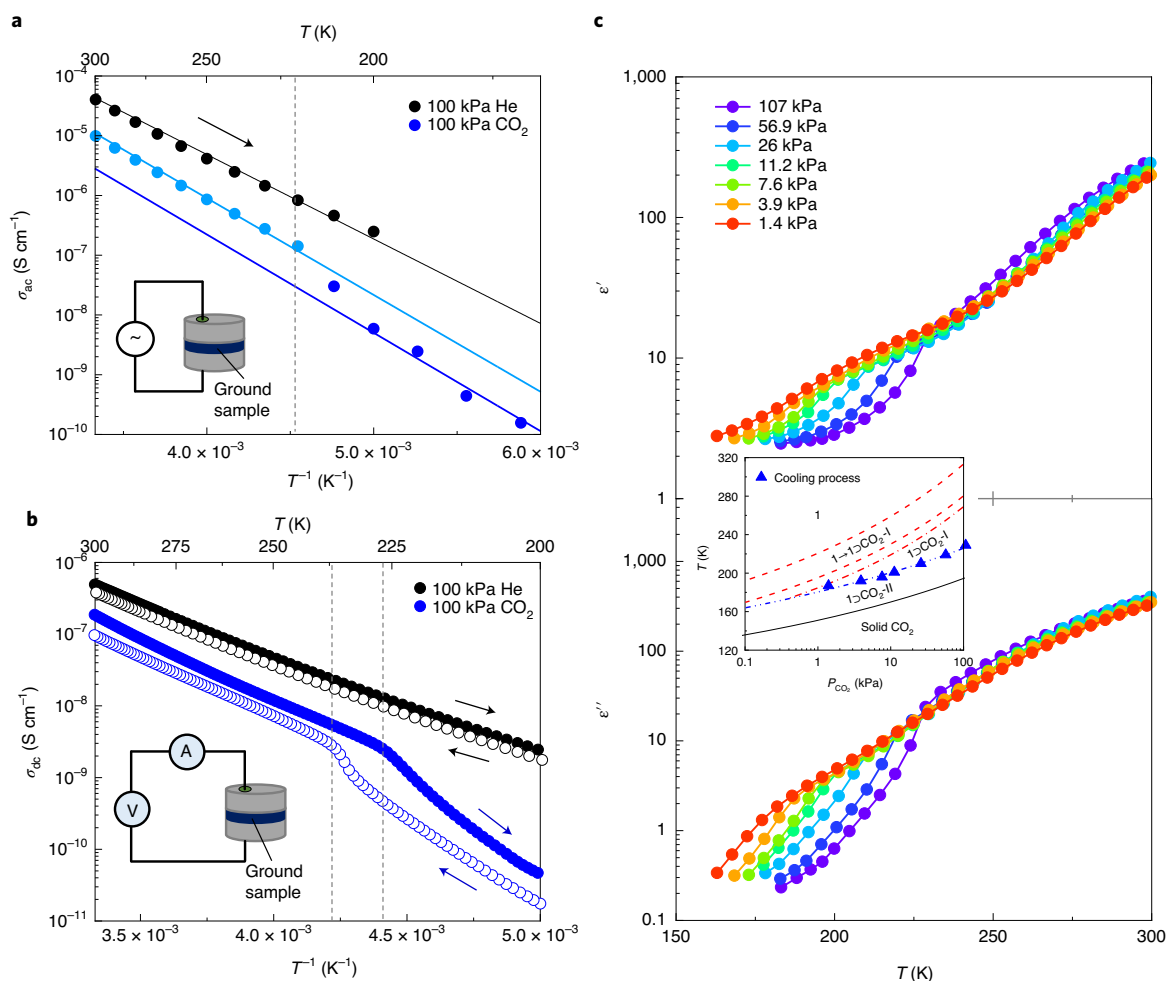


**Fig. 5 | Electronic properties responding to the phase transitions.** **a**, Arrhenius plots of  $\sigma_{ac}$  estimated from the Nyquist plots measured at several temperatures for a pelletized sample of **1** under  $P_{CO_2} = 100$  kPa of He (black) and  $CO_2$  (blue and azure), where the vertical dotted line indicates the 2nd GO transition. The black solid line represents the fitting based on the Arrhenius equation under 100 kPa of He, and the azure and blue solid lines represent similar fittings under 100 kPa of  $CO_2$  in the temperature ranges higher and lower than  $T_{IN}$ , respectively. **b**, Temperature dependence of  $\sigma_{ac}$  measured on a pelletized sample of **1** at several temperatures for **1** under  $P_{CO_2} = 100$  kPa of He (black) and  $CO_2$  (blue) for cooling (closed circles) and heating (open circles) processes, where the dotted lines indicate the 2nd GO/GC transitions. **c**, Temperature dependence of  $\epsilon'$  (top) and  $\epsilon''$  (bottom) of the dielectric constant for **1** measured during cooling under several  $CO_2$  pressures with an a.c. electric field frequency of 1 kHz. Inset: phase transition plots that display the 2nd GO transition estimated from the  $\epsilon''-T$  plot (the lines indicate the fitted lines in Fig. 2c).

To investigate the purpose of the  $CO_2$  atmosphere, the field-cooled magnetization and  $M-H$  curves were measured under lower  $CO_2$  pressures ( $P_{CO_2} = 1-10$  kPa); **1** was kept at 195 K for six hours, then cooled to 120 K with a sweep rate of 1 K  $min^{-1}$  and finally the magnetic measurements were conducted. At pressures of  $P_{CO_2} \leq 3$  kPa, magnetic ordering was still observed at around 110 K, but the  $M_s$  decreased while retaining the  $H_c$  (Fig. 4e,f). This indicated the partial formation of the  $1DCO_2-II$  phase in the crystals, even at low  $CO_2$  pressures. On increasing the  $CO_2$  pressure to 5 kPa, all the crystals transformed into the paramagnetic  $1DCO_2-II$  phase with  $M_s = 1.02 \times 10^3$  e.m.u.  $G mol^{-1}$  ( $0.18 N\mu_B$ ) under a 7 T field (Fig. 4f). The small  $M_s$  value compared with the expected value for two isolated isotropic  $S=1$  spins was attributed to the strong magnetic anisotropy (that is, zero-field splitting,  $D$ ) of  $[Ru^{II}, Ru^{III}]$  ( $D = 230-320$   $cm^{-1}$ ) (refs 42-44). Notably, the  $1DCO_2-I$  phase can be trapped at temperatures below  $T_{IN}$  without transition to  $1DCO_2-II$  by rapidly cooling from 300 to 120 K with a sweep rate of 10  $K min^{-1}$  under 5 kPa of  $CO_2$ . The trapped  $1DCO_2-I$  phase showed a ferrimagnetic phase transition at 88 K, as expected from the isostructural feature of **1-DCM** with  $T_c = 88$  K (Fig. 4g and Supplementary Figs. 32 and 33).

At  $P_{CO_2} = 100$  kPa, a sudden decrease in electronic conductivity was observed at around 220 K during the cooling process (Fig. 5a,b), which implies that the electronic state change from the one-electron-transferred state of  $1DCO_2-I$  to the neutral state of  $1DCO_2-II$  in the 2nd GO tends to suppress electron hopping over the framework. The heating process followed the cooling process with a temperature hysteresis ( $\Delta T_{IN} = 8$  K). In situ dielectric measurements with the real ( $\epsilon'$ ) and imaginary ( $\epsilon''$ ) parts of the permittivity showed the structural and electronic changes in the 2nd GO (Fig. 5c and Supplementary Fig. 35)<sup>45</sup>, which implies that the structural change in the 1st GO was not much and occurred gradually. The 2nd GO/GC  $T_{IN}$  agrees well with all the data in various  $CO_2$  atmospheres (inset of Fig. 5c and Supplementary Fig. 36).

To understand the stability of the electronic state in each form and the electronic and electrostatic effects of  $CO_2$  in  $1DCO_2-II$ , we carried out density functional theory calculations using four model structures that comprised the formula unit  $\{[Ru_2]\}-TCNQ(OEt)_2-\{Ru_2\}$  based on the results of single-crystal X-ray crystallography data for the present compounds: **1** (model A),  $1DCO_2-I$  without  $CO_2$  (model B),  $1DCO_2-II$  without  $CO_2$  (model C) and  $1DCO_2-II$

with CO<sub>2</sub> (model D) (Supplementary Fig. 37 and Supplementary Table 6). For each model, three electron configurations of ferromagnetic and ferrimagnetic states in the charge-distributed one-electron-transferred state ( $\{[Ru^{II}, Ru^{III}]-TCNQ(OEt)_2\}^{\cdot-}-[Ru^{II}, Ru^{III}]^{\cdot+}$ ) and the neutral state ( $\{[Ru^{II}, Ru^{III}]-TCNQ(OEt)_2\}-[Ru^{II}, Ru^{III}]\}$ ) were assumed (Supplementary Fig. 38). Experimentally, **1** and **1**▷CO<sub>2</sub>-**I** had a ferrimagnetic ground state of one electron transferred, whereas **1**▷CO<sub>2</sub>-**II** had the neutral ground state. The stabilization of the electron configuration state evaluated via theoretical calculations completely agreed with the ground state obtained experimentally (Fig. 6a and Supplementary Table 7). Furthermore, the neutral ground state of model D (with CO<sub>2</sub>) was much more stabilized ( $\Delta 15.4$  kcal mol<sup>-1</sup>) than that of model C (without CO<sub>2</sub>) despite being evaluated in the same  $\{[Ru^{II}, Ru^{III}]-TCNQ(OEt)_2\}-[Ru^{II}, Ru^{III}]\}$  skeleton. This was ascribed to the electronic effect of CO<sub>2</sub> molecules through frontier orbitals (the electrostatic effect on CO<sub>2</sub> molecules was also evaluated using a Hirshfeld charge model<sup>46</sup> (Supplementary Table 8), but it contributed little to the stabilization of the neutral state (Supplementary Table 7 and Supplementary Fig. 39). A particular emphasis is placed on the frontier orbitals in the neutral state of model D, where there is some interactions between an orbital of CO<sub>2</sub> and a  $\delta^*$  orbital of the [Ru(2)<sub>2</sub>] unit at the highest occupied molecular orbital 1 (HOMO-1) level and a  $\pi^*$  orbital of TCNQ(OEt)<sub>2</sub> unit at the lowest unoccupied molecular orbital (LUMO) level (Fig. 6b). These interactions can make the neutral state in **1**▷CO<sub>2</sub>-**II** more stable.

It is worth mentioning that **1** also adsorbed O<sub>2</sub> and a small amount of N<sub>2</sub> without changing its original electronic state (one-electron-transferred form) and the adsorbed amounts of O<sub>2</sub> and N<sub>2</sub> reached  $\sim 8$  mol mol<sup>-1</sup> (90 K) and  $\sim 1$  mol mol<sup>-1</sup> (120 K) at  $P_{O_2/N_2} = 100$  kPa, respectively (Supplementary Fig. 40). The profiles of the  $M-T$  and  $M-H$  curves at 1.8 K, for **1** under a N<sub>2</sub> atmosphere (100 kPa) were identical to those for the original **1** (Supplementary Fig. 43). However, their measurements under an O<sub>2</sub> atmosphere (100 kPa) were modified;  $T_C$  was decreased from 110 K in **1** to 88 K in **1**▷O<sub>2</sub> and the  $M-H$  curve at 1.8 K in **1**▷O<sub>2</sub> was largely deformed as a softer magnet with internal O<sub>2</sub> spins, as seen in the O<sub>2</sub>-accommodated layered antiferromagnet reported previously<sup>20</sup> (Supplementary Fig. 44). Meanwhile, the  $T_C$  in **1**▷O<sub>2</sub> was almost the same as that in **1**-DCM, so the  $T_C$  modification was due to a structural deformation caused by adsorbing/desorbing O<sub>2</sub>, similarly to that observed in the solvation process from **1** to **1**-DCM in addition to its structural stabilization.

## Conclusions

MOFs have previously been investigated for applications in carbon capture owing to their high CO<sub>2</sub> uptake and selectivity, although it is rare that they display CO<sub>2</sub>-induced changes in structure and properties<sup>47</sup>. In this work, we have demonstrated the reversible conversion of a guest-free ferrimagnetic MOF to a paramagnetic form when CO<sub>2</sub> guests were present in its pores. The guest-free ferrimagnet **1** with  $T_C = 110$  K first changed to the one-electron-transferred state **1**▷CO<sub>2</sub>-**I** with a  $\sim 4$  CO<sub>2</sub> uptake in the intra-layer hexagonal pores at  $P_{CO_2} < 5$  kPa, while still remaining ferrimagnetic, and, then, changed to the paramagnetic neutral state **1**▷CO<sub>2</sub>-**II** with the uptake of about another four CO<sub>2</sub> molecules in the newly opened interlayer pores at  $P_{CO_2} \geq 5$  kPa. Theoretical calculations using a density functional theory level suggested that the accommodated CO<sub>2</sub> molecules in the magnetic framework had a notable electronic effect. The interactions between the frontier orbitals of CO<sub>2</sub> and the host framework ( $\delta^*$  of the [Ru(2)<sub>2</sub>] unit and  $\pi^*$  of the TCNQ(OEt)<sub>2</sub> unit) allowed the stabilization of the paramagnetic neutral state in **1**▷CO<sub>2</sub>-**II**. This ability of the material to undergo electron transfer and structural transformations with the CO<sub>2</sub> uptake and release was associated with a change in its electronic conductivity and permittivity, which shows that MOFs can respond in a variety of manners

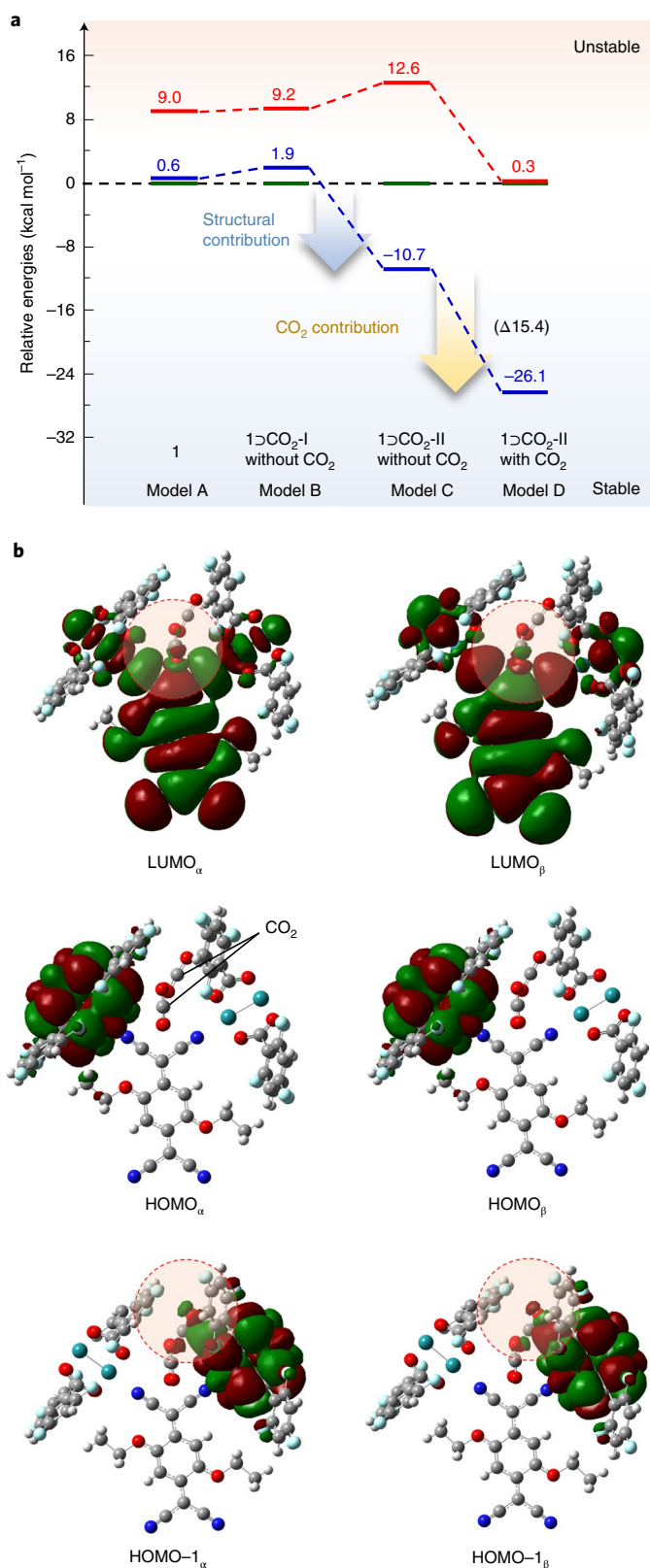


**Fig. 6 | Theoretical study on the stability of **1**▷CO<sub>2</sub>-**II**.** **a**, Relative energies among the ferromagnetic (red), ferrimagnetic (green) and neutral (blue) states in Models A–D, where the relative energies were normalized on the basis of the respective ferrimagnetic levels. **b**, Frontier orbitals of LUMO<sub>α/β</sub>, HOMO<sub>α/β</sub> and HOMO-1<sub>α/β</sub> levels in the Model D, where α and β indicate α and β spin configuration levels, respectively. The red dotted circles indicate the presence of meaningful interactions with CO<sub>2</sub>: TCNQ(OMe)<sub>2</sub>( $\pi^*$ )...CO<sub>2</sub> for LUMO<sub>α/β</sub> and [Ru<sub>2</sub>]( $\delta^*$ )...CO<sub>2</sub> for HOMO-1<sub>α/β</sub>.

to reaction-inert guest targets, such as CO<sub>2</sub> (ref. 48). These findings provide insights into understanding the mechanism by which switchable properties can be controlled by gas sorption, which may be helpful in future applications such as gas sensors or memory storages.

### Online content

Any methods, additional references, Nature Research reporting summaries, source data, extended data, supplementary information, acknowledgements, peer review information; details of author contributions and competing interests; and statements of data and code availability are available at <https://doi.org/10.1038/s41557-020-00577-y>.

Received: 4 July 2019; Accepted: 14 October 2020;

Published online: 30 November 2020

### References

- Kurmoo, M. Magnetic metal–organic frameworks. *Chem. Soc. Rev.* **38**, 1353–1379 (2009).
- Dechambenoit, P. & Long, J. R. Microporous magnets. *Chem. Soc. Rev.* **40**, 3249–3265 (2011).
- Coronado, E. & Espallargas, G. M. Dynamic magnetic MOFs. *Chem. Soc. Rev.* **42**, 1525–1539 (2013).
- Espallargas, G. M. & Coronado, E. Magnetic functionalities in MOFs: from the framework to the pore. *Chem. Soc. Rev.* **47**, 533–557 (2018).
- Miller, J. S. Magnetically ordered molecule-based materials. *Chem. Soc. Rev.* **40**, 3266–3296 (2011).
- Ohkoshi, S. et al. Photoinduced magnetization in copper octacyanomolybdate. *J. Am. Chem. Soc.* **128**, 270–277 (2006).
- Brataas, A., Kent, A. D. & Ohno, H. Current-induced torques in magnetic materials. *Nat. Mater.* **11**, 372–381 (2012).
- Lottermoser, T. et al. Magnetic phase control by an electric field. *Nature* **430**, 541–544 (2004).
- Ohkoshi, S., Arai, K., Sato, Y. & Hashimoto, K. Humidity-induced magnetization and magnetic pole inversion in a cyano-bridged metal assembly. *Nat. Mater.* **3**, 857–861 (2004).
- Kurmoo, M., Kumagai, H., Chapman, K. W. & Kepert, C. J. Reversible ferromagnetic–antiferromagnetic transformation upon dehydration–hydration of the nanoporous coordination framework, [Co<sub>2</sub>(OH)<sub>2</sub>(C<sub>4</sub>O<sub>4</sub>)<sub>2</sub>]<sub>n</sub>·3H<sub>2</sub>O. *Chem. Commun.* **24**, 3012–3014 (2005).
- Kaneko, W., Ohba, M. & Kitagawa, S. A flexible coordination polymer crystal providing reversible structural and magnetic conversions. *J. Am. Chem. Soc.* **129**, 13706–13712 (2007).
- Yoshida, Y., Inoue, K., Kikuchi, K. & Kurmoo, M. Biomimetic transformation by a crystal of a chiral Mn<sup>II</sup>–Cr<sup>III</sup> ferrimagnetic Prussian blue analogue. *Chem. Mater.* **28**, 7029–7038 (2016).
- Wang, Z.-M., Zhang, Y.-J., Liu, T., Kurmoo, M. & Gao, S. [Fe<sub>3</sub>(HCOO)<sub>6</sub>]<sub>n</sub>: a permanent porous diamond framework displaying H<sub>2</sub>/N<sub>2</sub> adsorption, guest inclusion, and guest-dependent magnetism. *Adv. Funct. Mater.* **17**, 1523–1536 (2007).
- Zeng, M.-H. et al. Nanoporous cobalt(II) MOF exhibiting four magnetic ground states and changes in gas sorption upon post-synthetic modification. *J. Am. Chem. Soc.* **136**, 4680–4688 (2014).
- Zhang, J., Kosaka, W., Sugimoto, K. & Miyasaka, H. Magnetic sponge behavior via electronic state modulations. *J. Am. Chem. Soc.* **140**, 5644–5652 (2018).
- Navarro, J. A. R. et al. Guest-induced modification of a magnetically active ultramicroporous, gismondine-like, copper(II) coordination network. *J. Am. Chem. Soc.* **130**, 3978–3984 (2008).
- Kaye, S. S., Choi, H. J. & Long, J. R. Generation and O<sub>2</sub> adsorption studies of the microporous magnets CsNi[Cr(CN)<sub>6</sub>]<sub>n</sub> (T<sub>C</sub> = 75 K) and Cr<sub>3</sub>[Cr(CN)<sub>6</sub>]<sub>2</sub>·6H<sub>2</sub>O (T<sub>N</sub> = 219 K). *J. Am. Chem. Soc.* **130**, 16921–16925 (2008).
- Bloch, E. D. et al. Hydrocarbon separations in a metal–organic framework with open iron(II) coordination sites. *Science* **335**, 1606–1610 (2012).
- Coronado, E., Gimenez-Marques, M., Espallargas, G. M. & Brammer, L. Tuning the magneto-structural properties of non-porous coordination polymers by HCl chemisorption. *Nat. Commun.* **3**, 828 (2012).
- Kosaka, W. et al. Gas-responsive porous magnet distinguishes the electron spin of molecular oxygen. *Nat. Commun.* **9**, 5420 (2018).
- Murphy, M. J. et al. Guest programmable multistep spin crossover in a porous 2-D Hofmann-type material. *J. Am. Chem. Soc.* **139**, 1330–1335 (2017).
- Halder, G. J., Kepert, C. J., Moubaraki, B., Murray, K. S. & Cashion, J. D. Guest-dependent spin crossover in a nanoporous molecular framework material. *Science* **298**, 1762–1765 (2002).
- Neville, S. M. et al. Guest tunable structure and spin crossover properties in a nanoporous coordination framework material. *J. Am. Chem. Soc.* **131**, 12106–12108 (2009).
- Coronado, E., Gimenez-Marques, M., Espallargas, G. M., Rey, F. & Vitorica-Yrezabal, I. J. Spin-crossover modification through selective CO<sub>2</sub> sorption. *J. Am. Chem. Soc.* **135**, 15986–15989 (2013).
- Zhou, H. C., Long, J. R. & Yaghi, O. M. Introduction to metal–organic frameworks. *Chem. Rev.* **112**, 673–674 (2012).
- Kitagawa, S., Kitaura, R. & Noro, S. Functional porous coordination polymers. *Angew. Chem. Int. Ed.* **43**, 2334–2375 (2004).
- Chu, S. Carbon capture and sequestration. *Science* **325**, 1599 (2009).
- Boot-Handford, M. E. et al. Carbon capture and storage update. *Energy Environ. Sci.* **7**, 130–189 (2014).
- Liao, P. Q., Huang, N. Y., Zhang, W. X., Zhang, J. P. & Chen, X. M. Controlling guest conformation for efficient purification of butadiene. *Science* **356**, 1193–1196 (2017).
- Kong, X. et al. Mapping of functional groups in metal–organic frameworks. *Science* **341**, 882–885 (2013).
- Farha, O. K. & Hupp, J. T. Rational design, synthesis, purification, and activation of metal–organic framework materials. *Acc. Chem. Res.* **43**, 1166–1175 (2010).
- McDonald, T. M. et al. Cooperative insertion of CO<sub>2</sub> in diamine-appended metal–organic frameworks. *Nature* **519**, 303–308 (2015).
- Sumida, K. et al. Carbon dioxide capture in metal–organic frameworks. *Chem. Rev.* **112**, 724–781 (2012).
- Thallapally, P. K. et al. Flexible (breathing) interpenetrated metal–organic frameworks for CO<sub>2</sub> separation applications. *J. Am. Chem. Soc.* **130**, 16842–16843 (2008).
- Carrington, E. J. et al. Solvent-switchable continuous-breathing behaviour in a diamondoid metal–organic framework and its influence on CO<sub>2</sub> versus CH<sub>4</sub> selectivity. *Nat. Chem.* **9**, 882–889 (2017).
- Diercks, C. S., Liu, Y., Cordova, K. E. & Yaghi, O. M. The role of reticular chemistry in the design of CO<sub>2</sub> reduction catalysts. *Nat. Mater.* **17**, 301–307 (2018).
- Niu, K. et al. A spongy nickel–organic CO<sub>2</sub> reduction photocatalyst for nearly 100% selective CO production. *Sci. Adv.* **3**, 1700921 (2017).
- Miyasaka, H. Control of charge transfer in donor/acceptor metal–organic frameworks. *Acc. Chem. Res.* **46**, 248–257 (2013).
- Miyasaka, H. in *Materials and Energy* (eds Vardeny, Z. V. & Wohlgenannt, M.) Ch. 4, 169–205 (World Scientific, 2018).
- Uemura, K., Kitagawa, S., Fukui, K. & Saito, K. A contrivance for a dynamic porous framework: cooperative guest adsorption based on square grids connected by amide–amide hydrogen bonds. *J. Am. Chem. Soc.* **126**, 3817–3828 (2004).
- Kosaka, W. et al. Magnetic sponge with neutral–ionic phase transitions. *Adv. Sci.* **5**, 1700526 (2018). (1–10).
- Cotton, F. A. & Walton, R. A. *Multiple Bonds Between Metal Atoms* 2nd edn (Oxford Univ. Press, 1993).
- Miyasaka, H. et al. Tuning of the ionization potential of paddlewheel diruthenium(II,II) complexes with fluorine atoms on the benzoate ligands. *Dalton Trans.* **40**, 673–682 (2011).
- Kosaka, W., Itoh, M. & Miyasaka, H. The effect of chlorine and fluorine substitutions on tuning the ionization potential of benzoate-bridged paddlewheel diruthenium(II, II) complexes. *Dalton Trans.* **44**, 8156–8168 (2015).
- Kosaka, W., Yamagishi, K., Zhang, J. & Miyasaka, H. Gate-opening gas adsorption and host–guest interacting gas trapping behavior of porous coordination polymers under applied a.c. electric fields. *J. Am. Chem. Soc.* **136**, 12304–12313 (2014).
- Hirshfeld, F. L. Bonded-atom fragments for describing molecular charge densities. *Theoret. Chim. Acta* **44**, 129–138 (1977).
- Yanai, N. et al. Gas detection by structural variations of fluorescent guest molecules in a flexible porous coordination polymer. *Nat. Mater.* **10**, 787–793 (2011).
- Kreno, L. E. et al. Metal–organic framework materials as chemical sensors. *Chem. Rev.* **112**, 1105–1125 (2012).

**Publisher's note** Springer Nature remains neutral with regard to jurisdictional claims in published maps and institutional affiliations.

© The Author(s), under exclusive licence to Springer Nature Limited 2020

## Methods

**Syntheses of 1-DCM and **1**.** All the synthetic procedures were performed under an inert atmosphere using standard Schlenk-line techniques and a commercial glove box. All the chemicals purchased from commercial sources were of reagent-grade quality. Solvents were distilled under N<sub>2</sub> using common drying agents. The starting material [Ru<sub>2</sub>(F<sub>3</sub>PhCO<sub>2</sub>)<sub>4</sub>(THF)<sub>2</sub>] (F<sub>3</sub>PhCO<sub>2</sub><sup>-</sup>, 2,4,6-trifluorobenzoate) was synthesized according to the previously reported method<sup>49</sup>. A solution (2 ml) of [Ru<sub>2</sub>(F<sub>3</sub>PhCO<sub>2</sub>)<sub>4</sub>(THF)<sub>2</sub>] (41.87 mg, 0.04 mmol) in DCM (20 ml) was carefully placed in narrow-diameter glass tubes (inner diameter of 8 mm) (bottom layer). Then, a mixed solvent of DCM/*p*-xylene in a volume ratio of 1:1 (1 ml) was added on the bottom layer as a buffer layer (middle layer). Finally, TCNQ(OEt)<sub>2</sub> (5.85 mg, 0.02 mmol) in *p*-xylene (20 ml) was separated into 2 ml portions and placed on the buffer layer of each tube (top layer). The glass tubes were left undisturbed for one week to yield block-shaped dark-brown crystals of **1-DCM** (yield, 54%). The crystallization solvents (3 molar amounts of DCM) in **1-DCM** were easily eliminated when the crystals were exposed only to air, as proved by thermogravimetric measurements (Supplementary Fig. 4), which made it difficult to accurately do elemental analyses for the **1-DCM** samples. Therefore, the elemental analysis for the present compound was performed only for the solvent-free dried sample **1**. Infrared (KBr),  $\nu$  (C≡N), 2,195, 2,161 cm<sup>-1</sup>.

Crystal samples of **1** were prepared by heating **1-DCM** at 353 K under vacuum for 12 h. Elemental analysis (%): calculated for C<sub>72</sub>H<sub>28</sub>F<sub>24</sub>N<sub>4</sub>O<sub>18</sub>Ru<sub>4</sub>, C (41.23), H (1.35), N (2.67). Found: C (41.64), H (1.44), N (2.72). Infrared (KBr):  $\nu$  (C≡N), 2,180, 2,131 cm<sup>-1</sup>.

**Physical measurements.** Infrared spectra were measured on a KBr pellet using a JASCO FT-IR 4200 spectrometer. Raman spectra were measured on a single crystal using a JASCO NRS-4500 Raman microscope. Thermogravimetric analyses were conducted on a Shimadzu DTG-60H apparatus under a N<sub>2</sub> atmosphere in the temperature range from 298 to 673 K at a heating rate of 5 K min<sup>-1</sup>. Differential scanning calorimetry was collected on a Shimadzu DSC-60 instrument in the temperature range 320–200 K with a sweep rate of 5 K min<sup>-1</sup> under a CO<sub>2</sub> flow of 50 ml min<sup>-1</sup> (general atmosphere pressure). PXRD patterns were collected on a Rigaku Ultima IV diffractometer with Cu K $\alpha$  radiation ( $\lambda$  = 1.5418 Å). Magnetic measurements were performed using a Quantum Design SQUID magnetometer (MPMS-XL) in the temperature and d.c. field ranges of 1.8 to 300 K and –7 to 7 T, respectively. Diamagnetic contributions were collected for the sample holder, Nujol and sample using Pascal's constants<sup>50</sup>. Fresh samples taken immediately from the mother liquids were used for the magnetic measurements of **1-DCM**, and the formula determined by single-crystal X-ray crystallography was used for data analyses. Electric properties were measured using a Keithley 2635A system source meter (d.c.) and an Andeen–Hagerling 2700A capacitance bridge, Solartron 1260 impedance and gain-phase analyser, and a Solartron 1296 dielectric interface (a.c.) with a temperature control using a Quantum Design PPMS system.

**In situ infrared spectra measurements.** In situ infrared spectra measurements were conducted through CaF<sub>2</sub> windows on a cryostat system (RC102, CRYO Industries) and connected to a gas-handling and pressure-monitoring system (BELSORP MAX, MicrotracBel) with a transmission configuration using a JASCO FT-IR 4200 spectrometer. Neat samples were sandwiched between two CaF<sub>2</sub> plates.

**In situ Raman spectra measurements.** In situ Raman spectra measurements were carried out in a JASCO NRS-4500 Raman microscope using a cryostat system (RC102, CRYO Industries) connected with a gas-handling and pressure-monitoring system (BELSORP MAX, MicrotracBel). Quartz and CaF<sub>2</sub> windows were equipped over the sample room and the vacuum insulating shield of the cryostat, respectively. The sample was inspected using an objective lens (Olympus SLMPLN20x) and was irradiated with a 532 nm Raman excitation laser.

**In situ PXRD spectra measurements.** A ground sample of **1** was sealed in a silica glass capillary with an inner diameter of 0.5 mm. The PXRD pattern was obtained with a 0.02° step using a Rigaku Ultima IV diffractometer with Cu K $\alpha$  radiation ( $\lambda$  = 1.5418 Å). To obtain the PXRD patterns under gas-adsorbed conditions, the glass capillary was connected to stainless-steel lines that possessed valves to dose and remove gas, which were connected to a gas-handling system (BELSORP MAX, MicrotracBel). The temperature was controlled by a N<sub>2</sub> gas stream.

**In situ CO<sub>2</sub> adsorption–magnetic measurements.** Polycrystalline samples were placed in a gelatin capsule. A piece of cotton was placed above the sample to prevent sample movement during the gas sorption process. Then, the capsule was held at the centre of a plastic straw. The straw was then attached on the edge of a homemade sample rod made of a SUS tube and a brass male thread with a fluorocarbon tape<sup>50</sup>. The sample was isolated from the surrounding atmosphere by overlaying a close-ended brass tube, which could be attached to the thread on the open end of the sample rod using screws. An airtight seal between the thread and brass tube was achieved using a silicon sealant (CAF 4, Bluestar Silicones). The SUS tube was connected to a gas-handling system with a turbo molecular pump and manometer (BELSORP MAX, Microtrac BEL). It was needless to subtract the background signal from the brass tube.

**CO<sub>2</sub> adsorption measurements.** The sorption isotherm and isobar measurements for CO<sub>2</sub> were carried out using an automatic volumetric adsorption apparatus (BELSORP MAX, MicrotracBel) connected to a cryostat system (ULVAC-Cryo). A known weight (~30 mg) of **1** was placed into the sample cell and then, prior to measurements, was evacuated using the degas function of the analyser for 12 h at 353 K. The change in the pressure was then monitored and the degree of adsorption determined by the decrease in the pressure at the equilibrium state.

**Crystallography.** Crystal data for **1-DCM**, **1**, **1**CO<sub>2</sub>-**I** and **1**CO<sub>2</sub>-**II** were collected at 103, 103, 195 and 195 K, respectively, on a CCD diffractometer (Rigaku Saturn724M) with multilayer mirror monochromated Mo K $\alpha$  radiation ( $\lambda$  = 0.71073 Å). Single crystals of **1-DCM** and **1** were mounted on a thin Kapton film using Nujol and cooled in a N<sub>2</sub> gas stream. For **1**CO<sub>2</sub>-**I** and **1**CO<sub>2</sub>-**II**, compound **1** was mounted on a thin glass capillary with a minimum amount of epoxy adhesive, which was attached to the inner wall of silica glass capillary with an inner diameter of 0.5 mm. The capillary was connected to gas-handling system through an O-ring seal connector, which can be fixed on a diffraction goniometer. CO<sub>2</sub> (3 kPa and 20 kPa) was introduced into the capillary at room temperature, then slowly cooled to 195 K by a N<sub>2</sub> gas stream to obtain **1**CO<sub>2</sub>-**I** and **1**CO<sub>2</sub>-**II**, respectively. All the structures were solved using direct methods SHELXT Version 2014/5<sup>51</sup> and expanded using Fourier techniques. Full-matrix least-squares refinements on *F*<sup>2</sup> were based on observed reflections and variable parameters, and converged with unweighted and weighted agreement factors of  $R_1 = \sum |F_o| - |F_c| / \sum |F_o|$  ( $I > 2.00\sigma(I)$ ) and  $wR_2 = [\sum (w(F_o^2 - F_c^2)^2) / \sum w(F_o^2)]^{1/2}$  (all data). The non-hydrogen atoms were refined anisotropically, and hydrogen atoms were refined using riding model. Structural diagrams were prepared using VESTA software<sup>52</sup>. The void volumes in the crystal structures were estimated using PLATON<sup>53</sup>.

To make an easier comparison among the structures, the unit cell axes of **1** and **1**CO<sub>2</sub>-**II** were transformed following vector alternations as  $\mathbf{a}' = \mathbf{a} - 2\mathbf{b} + \mathbf{c}$ ,  $\mathbf{b}' = -\mathbf{a} - \mathbf{c}$ ,  $\mathbf{c}' = \mathbf{a} - \mathbf{c}$  for **1** and  $\mathbf{a}' = \mathbf{a} + \mathbf{b} + 2\mathbf{c}$ ,  $\mathbf{b}' = -\mathbf{a} - \mathbf{b}$ ,  $\mathbf{c}' = \mathbf{a} - \mathbf{b}$  for **1**CO<sub>2</sub>-**II**, where  $\mathbf{a}$ ,  $\mathbf{b}$ , and  $\mathbf{c}$  are the standard axis vectors based on the IUCR rule, and  $\mathbf{a}'$ ,  $\mathbf{b}'$  and  $\mathbf{c}'$  are the transformed axis vectors with cell constants of  $a' = 25.047(2)$ ,  $b' = 17.6874(10)$ ,  $c' = 17.5621(10)$ ,  $\alpha' = 77.677(7)^\circ$ ,  $\beta' = 96.638(7)^\circ$ ,  $\gamma' = 111.780(8)^\circ$ ,  $V' = 7052.0(8)$ ,  $Z' = 4$  for **1** and  $a' = 24.891(3)$ ,  $b' = 17.8905(11)$ ,  $c' = 19.5665(10)$ ,  $\alpha' = 88.073(6)^\circ$ ,  $\beta' = 93.027(8)^\circ$ ,  $\gamma' = 92.382(8)^\circ$ ,  $V' = 8689.2(12)$ ,  $Z' = 4$  for **1**CO<sub>2</sub>-**II**, which are depicted as red arrows in Figs. 1d,e and 3c,d, and in Supplementary Figs. 2, 18 and 19. The unit cell transformation was not required for **1**CO<sub>2</sub>-**I**.

**In situ electric measurement.** A powder sample (~10 mg) was compressed into a pellet with a diameter of 10 mm and a thickness of ~0.1 mm and placed between two stainless-steel plates to create a parallel-plate capacitor to which Au wires were attached using Au paste. The capacitor was then placed in a cryostat system (PPMS, Quantum Design) equipped with coaxial cable for d.c. electrical resistivity, dielectric properties and impedance measurements, and connected to a gas-handling and pressure-monitoring system (BELSORP MAX, MicrotracBel). Prior to performing the analysis, the sample was dried under a high vacuum (<10<sup>-2</sup> Pa) at 353 K for 5 h. The d.c. electrical resistivity was measured by a two-probe method with a Keithley 2635 A system source meter with fixed source voltage at 0.1 V. Dielectric constants in the 0.1–10 kHz frequency range were measured using an Andeen–Hagerling 2700 A capacitance bridge with an input voltage amplitude that ranged from 0.2 to 15 V. Impedance measurements were performed over the frequency range from 10 to 100 kHz with a Solartron 1260 impedance and gain-phase analyser and a Solartron 1296 dielectric interface with a 1 V input voltage amplitude.

**Theoretical calculations.** For the four model structures (Models A–D) in Supplementary Fig. 37, density functional theory calculations were performed under the gas-phase condition by using the Becke 3-parameter Lee–Yang–Parr hybrid functional set<sup>54</sup>. As basis sets, LanL08(f) and 6-31G\* were used for Ru and other atoms, respectively<sup>55</sup>. The spin-polarized electronic structures were approximated by a spin-unrestricted broken symmetry method<sup>56,57</sup>. The Cartesian coordinates of those models that are summarized in Supplementary Table 6 are taken from the results of the X-ray crystallographic structural analyses for **1**, **1**CO<sub>2</sub>-**I** and **1**CO<sub>2</sub>-**II**. All the calculations were performed using the Gaussian09 program package<sup>58</sup>.

## Data availability

The data that support this work are available in the article and its Supplementary Information files. Further raw data are available from the corresponding authors upon reasonable request. X-ray crystallographic data have been deposited as CIFs at the Cambridge Crystallographic Data Centre (<http://www.ccdc.cam.ac.uk/>) with CCDC numbers 1914693 (**1-DCM**), 1914694 (**1**), 1914695 (**1**CO<sub>2</sub>-**I**) and 1914696 (**1**CO<sub>2</sub>-**II**). A copy of the data can be obtained free of charge via <https://www.ccdc.cam.ac.uk/structures/>. Source data are provided with this paper.

## References

- Miyasaka, H. et al. Tuning of the ionization potential of paddlewheel diruthenium (II, II) complexes with fluorine atoms on the benzoate ligands. *Dalton Trans.* **40**, 673–682 (2011).
- Boudreaux, E. A. & Mulay, L. N. *Theory and Application of Molecular Paramagnetism* (John Wiley & Sons, 1976).

51. Sheldrick, G. M. SHELXT: integrating space group determination and structure solution. *Acta Crystallogr. A* **70**, C1437 (2014).
52. Momma, K. & Izumi, F. VESTA 3 for three-dimensional visualization of crystal, volumetric and morphology data. *J. Appl. Cryst.* **44**, 1272–1276 (2011).
53. Spek, A. L. Single-crystal structure validation with the program PLATON. *J. Appl. Cryst.* **36**, 7–13 (2003).
54. Kitagawa, Y. et al. Theoretical studies on effects of hydrogen bonds attaching to cysteine ligands on 4Fe–4S clusters. *Int. J. Quant. Chem.* **108**, 2881–2887 (2008).
55. Roy, L. E., Hay, P. J. & Martin, R. L. Revised basis sets for the LANL effective core potentials. *J. Chem. Theory Comput.* **4**, 1029–1031 (2008).
56. Fukutome, H. The unrestricted Hartree–Fock theory of chemical reactions. I: The electronic instabilities in the chemical reactions and the solutions of the unrestricted SCF LCAO MO equation for the homopolar two-center two-electron system. *Prog. Theoret. Phys* **47**, 1156–1180 (1972).
57. Szabo, A. & Ostlund, N. S. *Modern Quantum Chemistry: Introduction to Advanced Electronic Structure Theory* (Dover, 1996).
58. Frisch, M. J. et al. *Gaussian 09 Revision C.01* (Gaussian, Inc., 2009).

## Acknowledgements

We thank H. Sato for his assistance with the single-crystal X-ray crystallography of the CO<sub>2</sub>-accommodated compounds. This work was supported by a Grant-in-Aid

for Scientific Research (nos 16H02269, 18K19050, 18K05055, 18H05208, 19K05401, 20K15294 and 20H00381) from MEXT, Japan, and on Innovative Areas (' $\pi$ -System Figuration' Area 2601, no. 17H05137) from JSPS, Japan, the GIMRT programme, the E-IMR project and a Grant Fund for Research and Education (no. J190001232). J.Z. is thankful for the JSPS KAKENHI (No. 17J02497).

## Author contributions

J.Z. and H.M. formulated the project. J.Z. performed the experiments. W.K. established the experimental set-ups, especially the measurements with the gases, and supported the experiments. Y.K. performed the theoretical calculations. All the authors contributed to the writing of the manuscript.

## Competing interests

The authors declare no competing interests.

## Additional information

**Supplementary information** is available for this paper at <https://doi.org/10.1038/s41557-020-00577-y>.

**Correspondence and requests for materials** should be addressed to H.M.

**Reprints and permissions information** is available at [www.nature.com/reprints](http://www.nature.com/reprints).